remote sensing

MDPI

Article

Response of Evapotranspiration (ET) to Climate Factors and Crop Planting Structures in the Shiyang River Basin, Northwestern China

Xueyi Yang [1,2], Xiaojing Shi [1,2], Yaling Zhang [1,2], Fei Tian [1,2,*] and Samuel Ortega-Farias [3]

[1] Center for Agricultural Water Research in China, China Agricultural University, Beijing 100083, China; s20213091783@cau.edu.cn (X.Y.); xiaojing06009@gmail.com (X.S.); sy20213091893@cau.edu.cn (Y.Z.)
[2] National Field Scientific Observation and Research Station on Efficient Water Use of Oasis Agriculture in Wuwei of Gansu Province, Wuwei 733000, China
[3] Research Program on Adaptation of Agriculture to Climate Change (A2C2), Research and Extension Center for Irrigation and Agroclimatology (CITRA), Faculty of Agricultural Sciences, Universidad de Talca, Campus Talca, Talca 3460000, Chile; sortega@utalca.cl
* Correspondence: feitian@cau.edu.cn; Tel.: +86-010-6273-6273

Abstract: Evapotranspiration (ET) is an essential part of energy flow between the surface of the earth and the atmosphere, simultaneously involving the water, carbon, and energy cycles. It is mainly determined by climate, land use, and land cover changes. Additionally, there is still a need for quantitative characterization of the impacts of climate factors and human activities on ET and regional water resource efficiency in arid and semiarid regions. Based on Landsat-8 remote sensing imagery and land use data, the crop planting structures in the Liangzhou District of the middle reaches of the Shiyang River Basin were identified using a multiband and multi-temporal approach in this study. Subsequently, the ET of major cash crops was inverted using the three-temperature model. This research quantitatively describes the responses of wheat and corn to the climate and human activities over a two-year period. Furthermore, the impact of crop planting structures and climatic factors on ET was elucidated. The results indicate that a combination of multi-temporal green and shortwave infrared 1 bands is the optimal spectral combination to extract the planting structures. Compared to 2019, the wheat area decreased by 23.27% in 2020, while the corn area increased by 5.96%. Both crops exhibited significant spatial heterogeneity in ET during the growing season. The typical daily range of ET for wheat was 0.4–7.2 mm/day, and for corn, it was 1.5–4.0 mm/day. Among the climatic factors, temperature showed the highest correlation with ET (R = 0.80, $p \leq 0.05$). Our research findings provide valuable insights for the fine identification of crop planting structures and a better understanding of the response of ET to climatic factors and planting structures.

Keywords: crop planting structures; evapotranspiration; remote sensing; climate factors

check for updates

Citation: Yang, X.; Shi, X.; Zhang, Y.; Tian, F.; Ortega-Farias, S. Response of Evapotranspiration (ET) to Climate Factors and Crop Planting Structures in the Shiyang River Basin, Northwestern China. *Remote Sens.* **2023**, *15*, 3923. https://doi.org/10.3390/rs15163923

Academic Editors: Ningbo Cui, Cong Wang, Taifeng Dong and Yulei Xie

Received: 16 June 2023
Revised: 25 July 2023
Accepted: 2 August 2023
Published: 8 August 2023

Copyright: © 2023 by the authors. Licensee MDPI, Basel, Switzerland. This article is an open access article distributed under the terms and conditions of the Creative Commons Attribution (CC BY) license (https://creativecommons.org/licenses/by/4.0/).

1. Introduction

Evapotranspiration (ET) is a crucial component of surface energy balance and water balance, consisting of soil evaporation and vegetation transpiration. It returns 58–65% of terrestrial precipitation to the atmosphere and transports 51–58% of surface energy from land through latent heat transfer [1,2]. Simultaneously, ET is regarded as the most important aspect of agricultural water allocation, with more accurate parameter values leading to more optimized farmland water strategies [3]. Traditional ET, primarily based on observations at stations, is obtained through point-scale field measurements, making it difficult to acquire regional-scale ET. However, remote sensing technology, with its wide coverage, periodicity, and timeliness, can effectively obtain large-scale ET [4]. Remote sensing-based ET estimation methods overcome the limitation of point observation. By using satellite sensors with high spatial and temporal resolution to obtain surface reflectance and combining it with multispectral, hyperspectral, and thermal infrared sensors on unmanned aerial

vehicle platforms, the accuracy of the ET estimation model can be effectively improved at the regional level. For instance, the three-temperature model (3T model) proposed by Qiu et al. [5,6] can effectively estimate ET and its components. The model requires fewer input parameters, which can be obtained through remote sensing inversion or meteorological stations. This model has been successfully applied for the quantitative characterization of ET at various scales in the northwest arid zone [7–9].

ET itself is affected by a variety of factors, such as crop type, crop growing conditions, soil conditions, and climate. However, changes in ET are mainly determined by climate, land use, and land cover change [10]. Regarding the driving mechanism of crop ET, the impact of climate and vegetation changes on ET has been a hot topic in the process of the terrestrial hydrological cycle [11–14]. Jin et al. [15] used the ET model to separate the effects of vegetation restoration and climate change on ET by controlling variables and found that vegetation restoration was the main driver of ET increase; He et al. [16] analyzed precipitation, potential ET, and ET based on the Budyko equation. They found that based on the average impact of vegetation restoration on ET changes, precipitation was the main driving factor for the ET changes. ET estimation and the hydrological models used by the above scholars can effectively evaluate the impact of climate and vegetation changes on ET changes. Still, there exist few studies on the effects of crop planting structure changes on ET under the broken and complex planting structure.

Identifying crop planting structures is vital to efficiently using agricultural water resources and supporting food security. The accurate monitoring of farmland information is also one of the central themes of agricultural remote sensing [17–19]. The classification of land use types in existing research has primarily been macroscopic, mainly divided into forestland, grassland, cultivated land, and urban land. However, most of the Liangzhou District (LD) focuses on developing agriculture, and there needs to be more quantitative research on the impact of different crop types on regional ET changes. Remote sensing data contains rich spectral geometry and texture features, which can distinguish the phenological characteristics, leaf pigment, leaf water content, and canopy structure of different crops so that the unique spectral reflection characteristics of other crops can be used to identify the planting structure [20].

The method of crop identification using remote sensing data has been updated and matured, and different satellite remote sensing images have their own advantages for crop identification at different temporal and spatial scales [21–26]. At the regional scale, high-resolution remote sensing data have shown better results for the identification of broken and complex planting structures [27–30]. Currently, crop remote sensing identification and classification methods can be distinguished based on the crop classification features and satellite image identification information used. The classification characteristics can mainly be divided into the following three categories: vegetation spectral information feature recognition [31], field texture feature recognition, and crop phenology information recognition [32]. Meanwhile, the identification information can be divided into satellite image-based spectral information [33] and multi-temporal information [34–36]. Using multisource remote sensing images (from Landsat-8 and Sentinel-2) based on supervised classification algorithms (the random forest algorithm and support vector machine algorithm) and an object-oriented segmentation algorithm (the recursive hierarchical segmentation algorithm), Xiong et al. [37] created a set of farmland distribution maps of 30 m in Africa from 2003 to 2014, and the overall accuracy reached 94%. Based on the spatiotemporal data fusion model, Chen et al. [38] in the typical agricultural areas of Hebei, Heilongjiang, and Xinjiang, the major planting provinces in northern China, used Landsat and MODIS images to construct a high spatiotemporal resolution image data set to explore the applicability of the spatiotemporal data fusion model in the field of agricultural information extraction.

The Shiyang River Basin, situated in the arid region of Northwest China, experiences limited rainfall, significant ET rates, extensive water resource development, and delicate natural ecology. Oasis farmland comprises approximately 10% of the total area in the Shiyang River Basin, with agricultural water being the foremost consumer of water re-

sources within the basin. Irrigated agriculture is developed in the LD, which is located in the oasis area in the middle reaches of the river basin. The mismatch between the supply and demand for agricultural water is the most prominent in this area. With the implementation of a water-saving reconstruction project, the ecological environment of the LD has been significantly improved, and the change in vegetation has had a direct or indirect impact on the regional hydrological cycle. Thus, under the combined effect of climate and planting structure changes, there is great significance in effectively evaluating the relative contribution rate of different influential factors on regional ET for the efficient use of water resources in the LD. However, the distribution of farmland in the LD has a certain complexity, with fragmented land plots and complex types. Therefore, it is necessary to find a method suitable for planting structure identification in the LD.

The objectives of this study are to (1) provide methods applicable to extracting typical crop planting structures in the middle reaches of the Shiyang River basin based on Landsat-8 high-resolution imagery; (2) quantitatively characterize the spatial and temporal variability of ET from typical crops under the influence of climate factors and crop planting structures based on the 3T model; and (3) investigate the driving factors of climate and planting structures for regional ET.

2. Materials and Methods

2.1. Study Area

The LD is located in Wuwei City, Gansu Province, Northwest China (101 59′–103 23′E, 37 23′–38 12′N), at the eastern end of the Hexi Corridor and the center of the Wuwei Oasis in the middle reaches of the Shiyang River Basin. The area is 5081 square kilometers, and the agricultural land is about 2155 square kilometers, accounting for 42.9% of the total area. The distribution of cropland in the study area is concentrated, and the area of farmland is relatively large. The terrain of this area is high in the southwest and low in the northeast, with an altitude of 1440–3263 m (Figure 1). This region belongs to the temperate continental arid climate, which is dry, with little rainfall and large temperature differences between day and night. The LD has typical dryland climate characteristics, with an average annual temperature of 7.7 °C, annual evaporation of 2020 mm, and average annual precipitation of 100 mm, which is far from sufficient to supply water for agricultural development. The area has 2873.4 h of sunshine and 139.05 kcal/cm^2 of total solar radiation. In recent years, the average temperature in the LD has exceeded the 1975–2015 average, making agricultural water use a more serious challenge in the context of climate change.

The development of agricultural resources dominates the LD. The main food crops are wheat and corn, which account for over 60% of the cropped area. These two types of bulk food crops are the main water-consuming crops, and their growth period is from April to September. In the cultivated land, a portion of vegetable cultivation area accounts for 1% to 4% of the land. However, due to the diverse types of cash crops and small and fragmented plots, this study categorizes them collectively as vegetables. The phenological stages of crops in the study area are listed as follows (Table 1).

Table 1. Phenological information of crop types.

Crop Type	April			May			June			July			August			September		
	E	M	L	E	M	L	E	M	L	E	M	L	E	M	L	E	M	L
Wheat	sow			grow			maturity			harvest								
Corn			sow				grow					maturity				harvest		
Veg.			sow											harvest				

Various growth stages of crops are represented using different colors. Encompassing various vegetables, the growth stages within Veg are intricate, with only the sowing and harvesting phases indicated in this table.

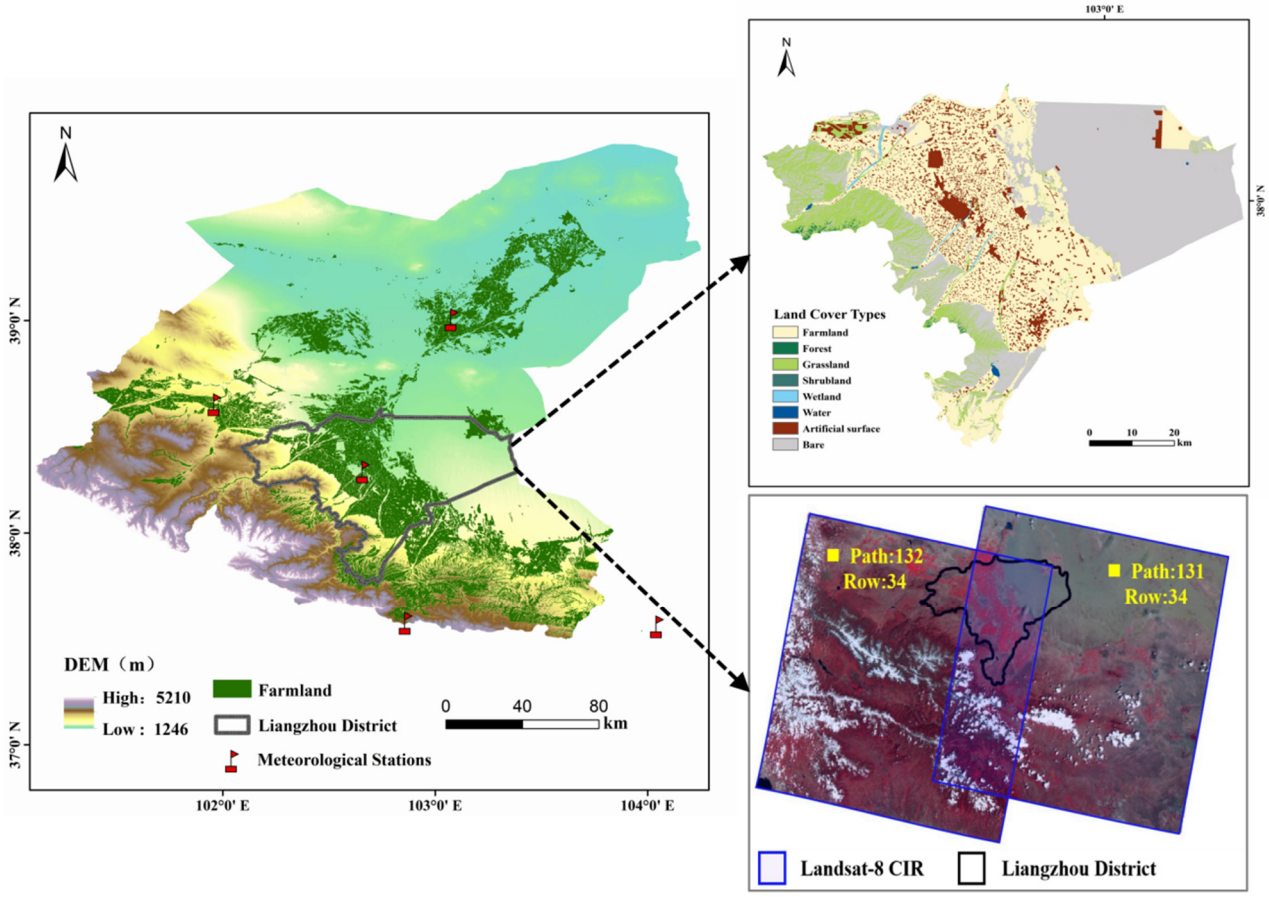


Figure 1. Study area of the Liangzhou District (LD). The LD is mosaicked by 2 Landsat-8 images.

2.2. Materials

2.2.1. Remote Sensing Data

Landsat-8 remote sensing images (Level 1T product, sourced from https://glovis.usgs.gov/, accessed on 1 September 2021) with a resolution of 30 m from NASA (the National Aeronautics and Space Administration) and the United States Geological Survey were used to collect satellite data, with a revisit period of 16 days. The acquired remote sensing data were first preprocessed, including radiometric calibration, atmospheric correction, and de-clouding. Then, all available images for the crop birth period (April–September) with path/row numbers 131/034 and 132/034 were considered for selection (Table 2). Due to the large volume of clouds during this period, only dates with less cloud interference during the crop fertility period could be selected, resulting in a total of 15 days (Table 2). Six spectral bands (B2–B7) of the Landsat-8 images were classified as feature bands (Table 3) and used, including the blue, green, red, near-infrared (NIR), shortwave infrared 1 (SWIR-1), and shortwave infrared 2 (SWIR-2) bands. This study mainly focused on the farmland system, so a 30 m spatial resolution land use data mask was downloaded from the National Tibetan Plateau Scientific Data Center (http://data.tpdc.ac.cn/zh-hans/, accessed on 1 September 2021).

Table 2. Summary of Landsat-8 images used in 2019–2020.

Year	Date	Day of Year (DOY)	Path/Row	Transit Time
2019	12 May	132	132/034	11:49
	21 May	141	131/034	11:43
	28 May	148	132/034	11:49
	6 June	157	131/034	11:43
	13 June	164	132/034	11:49
	24 July	205	131/034	11:43
	9 August	221	131/034	11:43
	25 August	237	131/034	11:43
	1 September	244	132/034	11:49
	26 Septrmber	269	131/034	11:43
2020	24 June	176	131/034	11:43
	1 July	183	132/034	11:49
	10 July	192	131/034	11:43
	17 July	199	132/034	11:49
	18 August	231	132/034	11:49

Table 3. Detailed information of 6 spectral bands.

Satellite	Band Name	Wavelength (nm)	Spatial Resolution (m)
Landsat-8 OLI	Blue (B2)	450–515	30
Landsat-8 OLI	Green (B3)	525–600	30
Landsat-8 OLI	Red (B4)	630–680	30
Landsat-8 OLI	NIR (B5)	845–885	30
Landsat-8 OLI	SWIR-1 (B6)	1560–1660	30
Landsat-8 OLI	SWIR-2 (B7)	2100–2300	30

2.2.2. Meteorological Data

Daily meteorological data including temperature (Ta), precipitation (P), and relative humidity (RH) were taken from the China Meteorological Data Network (http://data.cma.cn, accessed on 1 October 2021). Meanwhile, we gathered meteorological data from the meteorological stations around the LD (Table 4).

Table 4. General information about meteorological stations.

Station No.	Station Name	Longitude	Latitude	Altitude (m)
52681	Minqin	103°08′	38°63	1367.8
52674	Yongchang	101°97′	38°23	1976.9
52679	Wuwei	102°67′	37°92	1531.5
52787	Wushaoling	102°87′	37°02	3045.1
52797	Jingtai	104°05′	37°18	1630.9

Figure 2 shows data on climatic variables for the crop growing season. The monthly average precipitation during the growing season was 24.17 mm and 27.51 mm in 2019 and 2020, respectively. In 2019 the peak was at 51.40 mm in July, while in 2020 the peak was at 55.60 mm in September. The monthly temperatures during the growing season ranged from 11.45 °C to 21.89 °C, with a mean value of 17.75 °C in 2019 and 17.85 °C in 2020. Meanwhile, the annual mean value of the vapor pressure difference (VPD) showed an increasing trend, with the lowest value of 0.82 KPa occurring in September 2020 and the highest value of 1.57 KPa occurring in June of the same year. In general, variations in the meteorological data from the LD represent the typical seasonal trend in the northwest arid zone.

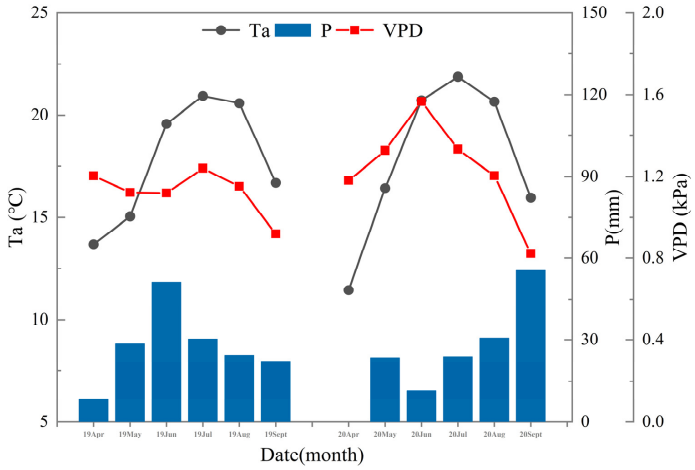


Figure 2. Monthly variations in temperature (Ta), precipitation (P), and vapor pressure difference (VPD) during the study period.

2.2.3. Sample Data

Sample plots were selected and identified to ensure the accuracy of crop classification by combining ground sampling points with the visual interpretation of high spatial resolution images on Google Earth Pro. During the experiment, a total of 247 sample plots were extracted in the study area, and a total of 5632 pixels were used as ground truth datasets for model training and accuracy evaluation. The ground sampling points were randomly divided into two parts: 2/3 for model training and 1/3 for accuracy validation (Table 5).

Table 5. General information about the sample plots.

Crop Types	Number of Training Plots	Number of Testing Plots	Number of Training Pixels	Number of Testing Pixels
Wheat	72	37	2384	665
Corn	96	42	3248	963

2.3. Data Analysis

2.3.1. Crop Classification Method

Two classification experiments were designed to study and analyze the effects of different spectral bands and temporal combinations on crop classification results (Figure 3): First, for single-band multi-temporal combinations, crop classification was performed using single-band analysis based on multi-temporal conditions, which were mutually validated with the results from Experiment 2. Second, for multiband multi-temporal combinations, the aim was to investigate how combinations of different wavebands affect the performance of a classification model under multi-temporal conditions. The band combinations were categorized into five groups. The first group comprised two band combinations randomly selected from the B2–B7 bands of the Operational Land Imager (OLI) images, with a total of 15 combinations. The second group included three band combinations, totaling 20 combinations. The third group had 4 band combinations, with a total of 15 combinations. The fourth group comprised five band combinations with six possibilities. Finally, the fifth group included all bands in the OLI images, with only one combination. The classification effects of these 57 band combinations differed, allowing us to determine the sensitive bands and the best classification combinations for crop classification. Because the sensitivity of crops to different band combinations varies, this experiment can identify the optimal band combinations for effective crop classification. The accuracy of the classification experiments was evaluated by a confusion matrix. Random forest classification was conducted using two Python modules: pandas and scikit-learn. The classification process was designed to have good noise immunity by following the random and put-back principles during sampling.

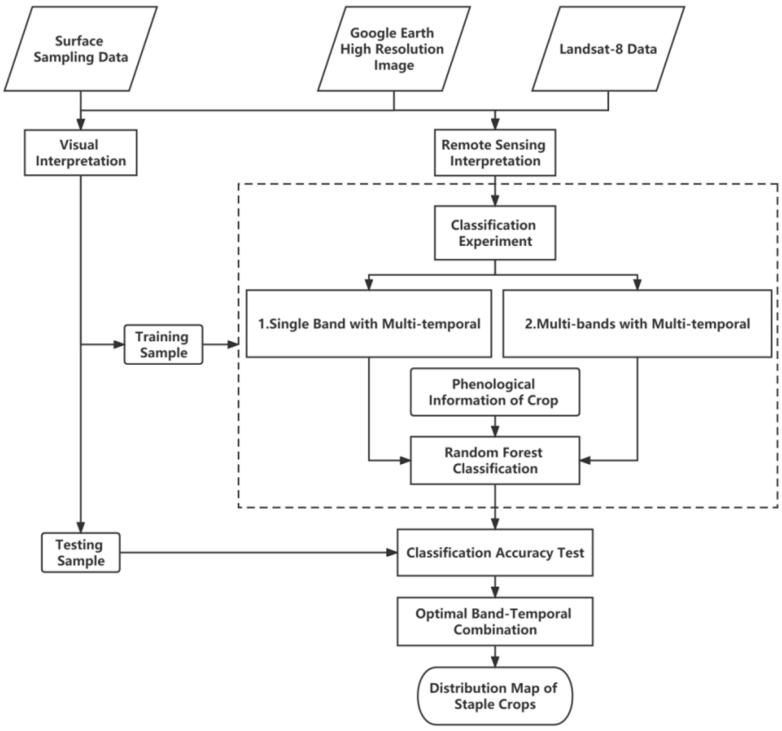


Figure 3. The workflow of crop classification using the random forest method.

2.3.2. Evapotranspiration Remote Sensing Estimation Method

The 3T model and satellite remote sensing images were employed in the study to calculate ET. Qiu et al. [5,6,39] proposed the 3T model to measure ET and evaluate environmental quality based on the surface energy balance equation in recent years. The model's input parameters are three temperatures, net radiation, and soil heat flux, with all parameters except air temperature being obtainable by direct inversion of remote sensing data. The 3T model consists of two submodels: the soil evaporation submodel and the vegetation transpiration submodel. For the mixed zone of vegetation and soil, the model assigns weights to soil evaporation and vegetation transpiration according to the vegetation cover values and calculates the total transpiration. This model has been widely used in arid and semiarid regions and has yielded favorable results in the northwest dry zone [40,41].

Submodel of Soil Evaporation

The 3T Model is a mature model, and here, we only introduce the principles and two submodels. The 3T model is implemented based on the surface energy balance equation.

$$\lambda E = R_n - G - H \tag{1}$$

where λE is the latent heat flux ($W \cdot m^{-2}$), λ is the latent heat of the vaporization of water vapor, and E is the evapotranspiration. R_n is the net radiation flux ($W \cdot m^{-2}$), G is the soil heat flux ($W \cdot m^{-2}$), and H is the sensible heat flux that can be calculated by the following equation:

$$H = \frac{\rho C_p (T_s - T_a)}{r_a} \tag{2}$$

where ρ is the air density ($kg \cdot m^{-3}$), C_p is the specific heat at constant pressure ($MJ \cdot kg^{-1} \cdot K^{-1}$), T_s is the soil surface temperature (K), T_a is the air temperature (K) and r_a is the aerodynamic resistance ($s \cdot m^{-1}$).

The concept of reference soil (dry soil without moisture evaporation) and reference vegetation was introduced by Qiu et al. [5,42,43]. They proposed that the reference soil and reference vegetation have the same atmospheric conditions in terms of air temperature,

humidity, and wind speed at the reference height as the surrounding soil and vegetation. This implies that the aerodynamic resistance is the same for both the reference soil and reference vegetation, and the ordinary evaporating soil and transpiring vegetation ($r_a = r_{a,sd}$, $T_a = T_{a,sd}$). The reference soil has no evaporation, and the reference vegetation has no transpiration, resulting in an approximate latent heat flux of zero, so the r_a can be estimated as:

$$r_a = r_{a,sd} = \frac{\rho C_p (T_{sd} - T_a)}{R_{n,sd} - G_{sd}} \tag{3}$$

where T_{sd} is the surface temperature of the reference soil (K), $R_{n,sd}$ is the net radiation flux of the reference soil (W·m^{-2}), and G_{sd} is the reference soil heat flux (W·m^{-2}).

By combining Equations (1)–(3), the soil evaporation can be estimated as follows:

$$\lambda E_s = R_{n,s} - G_s - (R_{n,sd} - G_{sd}) \frac{T_s - T_a}{T_{sd} - T_a} \tag{4}$$

where λE_s is the latent heat flux of soil evaporation (W·m^{-2}), E_s is soil evaporation. $R_{n,s}$ is the net radiation flux of the surface (W·m^{-2}) and G_s is the soil heat flux (W·m^{-2}).

Submodel of Transpiration of Vegetation

With the same method, when vegetation completely covers the land surface, soil heat flux G can be ignored, and the reference vegetation canopy temperature is introduced to calculate vegetation transpiration:

$$\lambda E_c = R_{n,c} - R_{n,cp} \frac{T_c - T_a}{T_{cp} - T_a} \tag{5}$$

where λE_c is the latent heat flux of transpiration (with λ being the latent heat of the vaporization of water vapor and E_c being the transpiration of vegetation), $R_{n,c}$ is the net radiation of the vegetation canopy (MJ·m^{-2}), T_c is the canopy temperature (K), $R_{n,cp}$ is the net radiation flux absorbed by the reference vegetation (MJ·m^{-2}), and T_{cp} is the canopy temperature (K) of the reference vegetation.

Vegetation–Soil Mixed Zone Model

When the ground surface is a mixed area of vegetation and soil, vegetation coverage is introduced to calculate the total ET by combining the above two submodels:

$$ET = (1 - f) \times E_s + f \times E_c \tag{6}$$

where f is the fractional vegetation coverage.

Vegetation Index and Fractional Vegetation Cover

The ET estimation of mixed pixels is a difficult point in the application of this model. The normalized difference vegetation index ($NDVI$) is considered to be the most effective vegetation index for judging whether the underlying surface is a pure pixel. When the $NDVI$ of a pixel is less than or equal to $NDVI_{min}$, the area is a pure soil pixel; when the $NDVI$ of a pixel is greater than or equal to $NDVI_{max}$, the area is a pure vegetation pixel; and when the $NDVI$ is between $NDVI_{min}$ and $NDVI_{max}$, the area is a mixed pixel. Among them, $NDVI_{min}$ and $NDVI_{max}$ represent the $NDVI$ of bare soil and complete vegetation coverage and generally take the mean value of 3% at both ends of the $NDVI$ frequency histogram [44]:

$$NDVI = \frac{NIR - R}{NIR + R} \tag{7}$$

$$f = \frac{NDVI - NDVI_{\min}}{NDVI_{\max} - NDVI_{\min}} \tag{8}$$

In the equation, the *NIR* and *R* represent the reflectance of Landsat-8 imagery corresponding to B5 (the *NIR* band) and B4 (the red band), respectively.

Land Surface Temperature

We used a single-channel algorithm for the estimation of surface temperature [45]:

$$LST = \frac{T_{sensor}}{1 + (\lambda T_{sensor}/A)\ln \varepsilon_0} \tag{9}$$

where LST is the land surface temperature (K); λ is the central wavelength of the thermal infrared band (um); A is the product of the Planck constant and the speed of light divided by the Boltzmann constant (the value is 1.439×10^4 um K); T_{sensor} is the brightness temperature (K), which is obtained by direct calibration of the B10 band of the Landsat-8 image; and ε_0 is the surface-specific emissivity.

Net Solar Radiation

The R_n refers to the radiation difference obtained after subtracting the part reflected by the surface from the total solar radiation reaching the surface. It is calculated by Equation (7):

$$R_n = R_{swd} - R_{swu} + R_{lwd} - R_{lwu} \tag{10}$$

where R_{swd} and R_{swu} represent the absorbed and released shortwave radiation ($W \cdot m^{-2}$), respectively, and R_{lwd} and R_{lwu} represent the absorbed and released longwave radiation ($W \cdot m^{-2}$), respectively. All the above parameters can be obtained by remote sensing estimation.

Soil Heat Flux

Soil heat flux (G) is calculated from the relationship between vegetation and net solar radiation:

$$G = R_n[\Gamma_c + (1 - f)(\Gamma_s - \Gamma_c)] \tag{11}$$

where Γ_c and Γ_s are the empirical coefficients, which are, respectively, 0.05 and 0.315. [46,47].

Net Solar Radiation of Reference Surface

The reference net radiation refers to the solar radiation absorbed by a specific pixel identified as either soil or vegetation when its temperature reaches the reference temperature. It can be calculated using Equation (12), where the albedo and surface emissivity in the equation should be replaced with the values for bare soil or vegetation, respectively, to obtain the reference net radiation absorbed by the reference soil and the reference vegetation [7].

$$R_{n,r} = (1 - \alpha_r)R_{swd} + \varepsilon_{0r}\varepsilon_a \sigma T_r^4 \tag{12}$$

where r denotes the reference surface. For the reference soil and reference vegetation, the values of α_r are 0.275 and 0.225 [39,48]; the values of ε_{0r} are 0.97 and 0.99 [5,48], respectively, for the emissivity; and the reference soil temperature and the reference vegetation temperature.

Temperature of Reference Surface

The reference temperature refers to the theoretical temperature of an image pixel when evaporation or transpiration is zero. Numerous studies have demonstrated that the highest point of surface temperature in remote sensing imagery can best represent the reference temperature. Firstly, the soil temperature and vegetation temperature are separated from the remotely sensed surface temperature. Then, the maximum value of each is taken as the reference temperature value [49].

Soil Heat Flux of Reference Surface

$$G = 0.315 R_{n,sd} \tag{13}$$

2.3.3. Timescale Expansion of Evapotranspiration

Satellite remote sensing images can only record instantaneous values at the time of transit, and the ET obtained by 3T model estimation is also an immediate value. In order to understand the actual water consumption during crop growth, daily ET values need to be obtained by extending the transient values on a daily scale. This study used the empirical formula of Jackson et al. [50] to extend the instantaneous ET values to daily ET values according to the time-step integration method as follows:

$$ET_d = \frac{2N_e(ET_i)}{\pi \sin(\pi t_i / N_e)} \quad (14)$$

where ET_d is the daily ET; ET_i is the instantaneous ET; $N_e = N - 2$, with N being the time interval from sunrise to sunset; and t_i is the time interval from the beginning of the ET process in the early morning to time i (the satellite transit time).

2.3.4. Data Analysis

To quantitatively characterize the impact of crop planting structures, the mask was created in QGIS using the results of crop planting structure classification, and an analysis of spatial and temporal variation in ET for two primary cereal crops was conducted. Meanwhile, spatial interpolation was conducted for climate factors Ta, P, and VPD. All analyses were pixel-based with a spatial resolution of 30 m. Pearson correlation analysis [51] was used to determine the correlation between each climatic factor and ET. The closer the value of $R(a,b)$ is to 1 or -1, the stronger the correlation between the two variables. The formula is as follows:

$$R(a,b) = \frac{E(ab)}{\sigma_a \sigma_b} \quad (15)$$

where a and b be two zero-mean real-valued random variables, $E(ab)$ is the cross-correlation between a and b.

3. Results

3.1. Crop Identification

To demonstrate that incorporating multi-temporal information can enhance classification accuracy, the efficacy of multi-temporal information was initially assessed before constructing the classification model. A comparison was conducted between single-temporal, two-temporal, and multi-temporal images using a random forest classification model with temporal data from the day of year DOY 148, DOY164, and DOY244. The findings reveal that the classification accuracy of the multi-temporal data combination surpasses that of the single-temporal data combination by 6.93% to 9.53% and exceeds that of the two-temporal data combination by 2.93% to 5.44% (Table 6). Consequently, in subsequent classification Experiments 1 and 2, all classification analyses were performed based on multi-temporal images.

Table 6. The overall accuracy of different temporal combinations for crop classification.

Number of Temporal	Date	Overall Accuracy	Kappa Coefficient
1	DOY148	90.00%	0.84
1	DOY164	87.40%	0.79
1	DOY244	89.95%	0.84
2	DOY148, DOY164	91.49%	0.86
2	DOY148, DOY244	92.60%	0.88
2	DOY164, DOY244	94.00%	0.90
3	DOY148, DOY164, DOY244	96.93%	0.95

3.1.1. Classification Experiment 1: Single Band with Multi-Temporal

In Experiment 1, images from three typical dates representing different crop fertility periods (DOY148, DOY164, and DOY244) were selected for the classification experiment. The accuracy of the results is presented in Figure 4. The results show that the green band has the highest accuracy, while the NIR band's and SWIR-2 band's classification accuracy is lower.

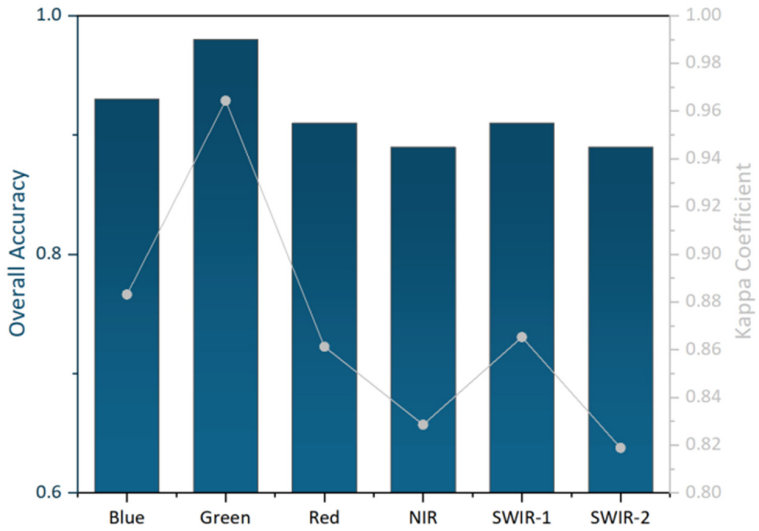


Figure 4. Crop classification accuracy with single-band and multi-temporal information.

3.1.2. Classification Experiment 2: Multi-Band with Multi-Temporal

Figure 5 illustrates the overall accuracy of each band combination, with the abscissa representing the number of bands used in classification training, with 15 combinations when choosing any two bands out of B2 to B7 from the OLI image, 20 combinations when choosing any three bands, and so on. The experimental results reveal that as the number of bands increases, the highest classification accuracy tends to decrease, while the lowest classification accuracy exhibits an increase. The peak value emerges in the two bands combination, reaching 97.77%. Although the overall accuracy of the six bands combination remains impressive at 96.93%, it does not represent the maximum value. The addition of band information does not effectively enhance classification accuracy.

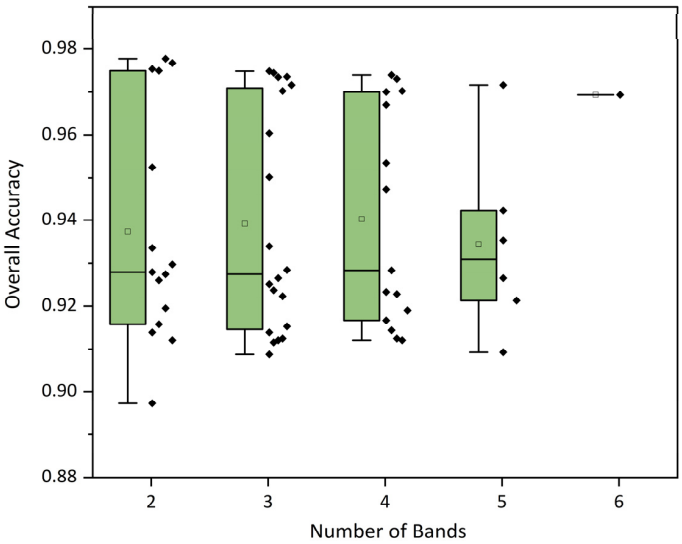


Figure 5. Crop classification's overall accuracy with different band number combinations. The scatter plot in the figure represents the overall accuracy for different band combinations.

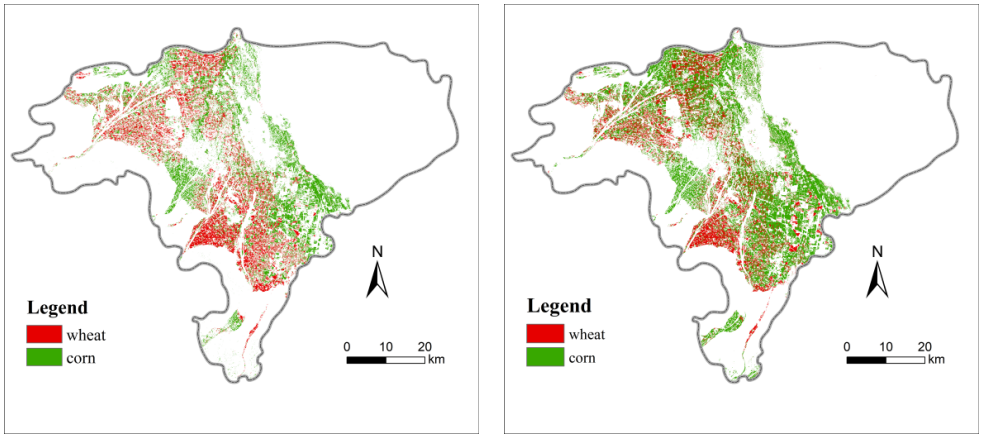
Furthermore, it can be observed that the band combinations achieving the highest classification accuracy consistently include green bands. This finding aligns with the results presented in the single band multi-temporal, as shown in Table 7. Consequently, the green and SWIR-1 bands constitute the most sensitive combination for crop classification for the study area.

Table 7. The best band combination of different band combinations for crop classification.

Number of Band Combination	Band of Landsat-8 OLI	Overall Accuracy	Kappa Coefficient
2	Green, SWIR-1	97.77%	0.96
3	Blue, Green, Red	97.48%	0.96
4	Blue, Green, Red, SWIR-2	97.39%	0.96
5	Blue, Green, Red, SWIR-1, SWIR-2	97.16%	0.95
6	Blue, Green, Red, NIR, SWIR-1, SWIR-2	96.93%	0.95

3.1.3. Crop Classification Result in the Liangzhou District

The aforementioned experimental analysis identified a combination of two spectral bands (green and SWIR-1) from three periods (DOY148, DOY164, and DOY244) as the optimal feature set to identify wheat and corn within the study area. The crop distribution map for the LD in 2019 was obtained using the classification model (Figure 6a). The evaluation of the confusion matrix for the random forest classification using the optimal feature set is presented in Table 8. The overall accuracy reached 97.77%. To further investigate the interannual adjustments in the planting structure of major crops and elucidate the annual variations in agricultural water consumption, the spatial distribution of wheat and corn in the study area for the year 2020 was extracted using the optimal classification feature set obtained (Figure 6b). The results of the planted area for wheat and corn in 2019 and 2020 are presented in Table 9. In 2020, the planted area of wheat was 24.241 kha, which had decreased by 7.353 kha compared to 31.594 kha in 2019. The planted area of corn was 47.322 kha, which had increased by 2.817 hectares compared to 44.505 kha in 2019.



(**a**) (**b**)

Figure 6. Wheat and corn distribution map extracted from Landsat-8 Operational Land Imager (OLI) data in the Liangzhou District (LD): (**a**) the result for 2019, and (**b**) the result for 2020.

Compared with the data in the Gansu Provincial Statistical Yearbook, the accuracy of the classification results for wheat in 2019 was 92.58%, the accuracy for corn in 2019 was 98.25%, the accuracy for wheat in 2020 was 85.82%, and the accuracy of corn in 2020 was 96.70%.

Table 8. Confusion matrix for random forest classification using green and SWIR-1 band combined features.

Crop Types	Classification Results			Total	Producer Accuracy
	Wheat	Corn	Others		
Wheat	646	0	0	646	97.14%
Corn	19	963	29	1011	100.00%
Others	0	0	493	493	94.44%
Total	665	963	522	2150	
User Accuracy	100.00%	85.25%	100		
Overall Accuracy = 97.77% Kappa = 0.96					

Table 9. Changes in the wheat and corn planting area in the Liangzhou District (LD) from 2019 to 2020.

Crop Types	2019		2020		Change in Area
	Number of Pixels	Area (kha)	Number of Pixels	Area (kha)	
Wheat	351,221	31.594	269,483	24.241	−7.353
Corn	494,747	44.505	526,061	47.322	2.817
Total	845,968	76.099	795,544	71.563	−4.536

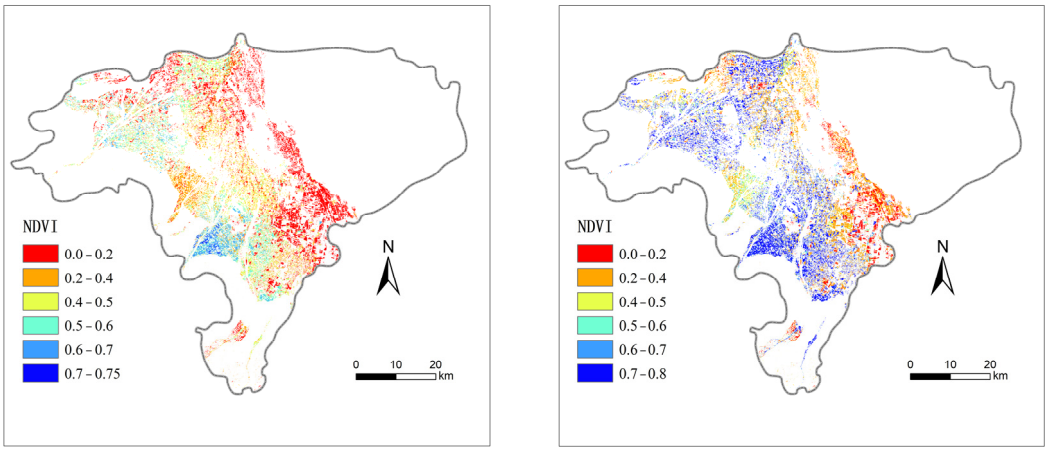
3.2. Evapotranspiration Estimation

3.2.1. Key Model Parameters Estimation

The input parameters of the 3T model were estimated for typical dates of the different growth stages (12 May, 28 May, 13 June, and 1 September 2019), resulting in the spatial distribution of parameters such as the NDVI and LST based on crop mask extraction.

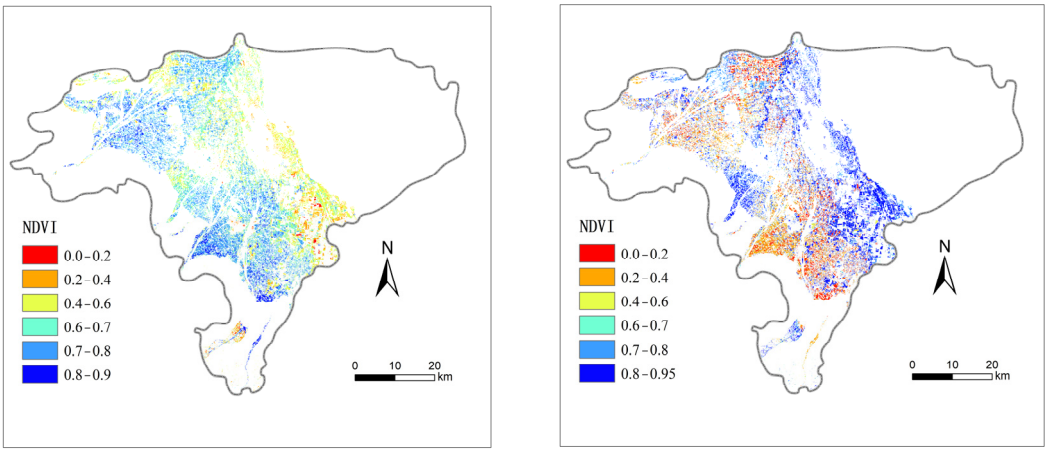
The distribution diagrams for the NDVI highlight the distinctions in phenological stages among different crops (Figure 7). On 12 May, the NDVI values in the wheat region were primarily distributed between 0.5 and 0.7, while the NDVI values in the corn region were below 0.4. Over time, the NDVI values exhibited a gradual increase. On 13 June, the wheat flourished, with the NDVI value reaching approximately 0.8. By 1 September, the wheat had been harvested, and the NDVI in the original wheat distribution area had diminished. Concurrently, the corn area reached a peak of 0.95.

The LST exhibited pronounced spatial heterogeneity and is strongly correlated with vegetation coverage (Figure 8). In areas with low vegetation coverage, such as Changcheng town (102°54′, 37°54′), which is surrounded by desert, the temperature is higher due to the exposed surface. As the crop growing season progresses, the LST shows an increasing trend, with a minimum value of 280 K and a maximum value of 315 K. During these four periods, the LST in the wheat area is consistently lower than that in the corn area, primarily influenced by the leaf morphology of the two plants.



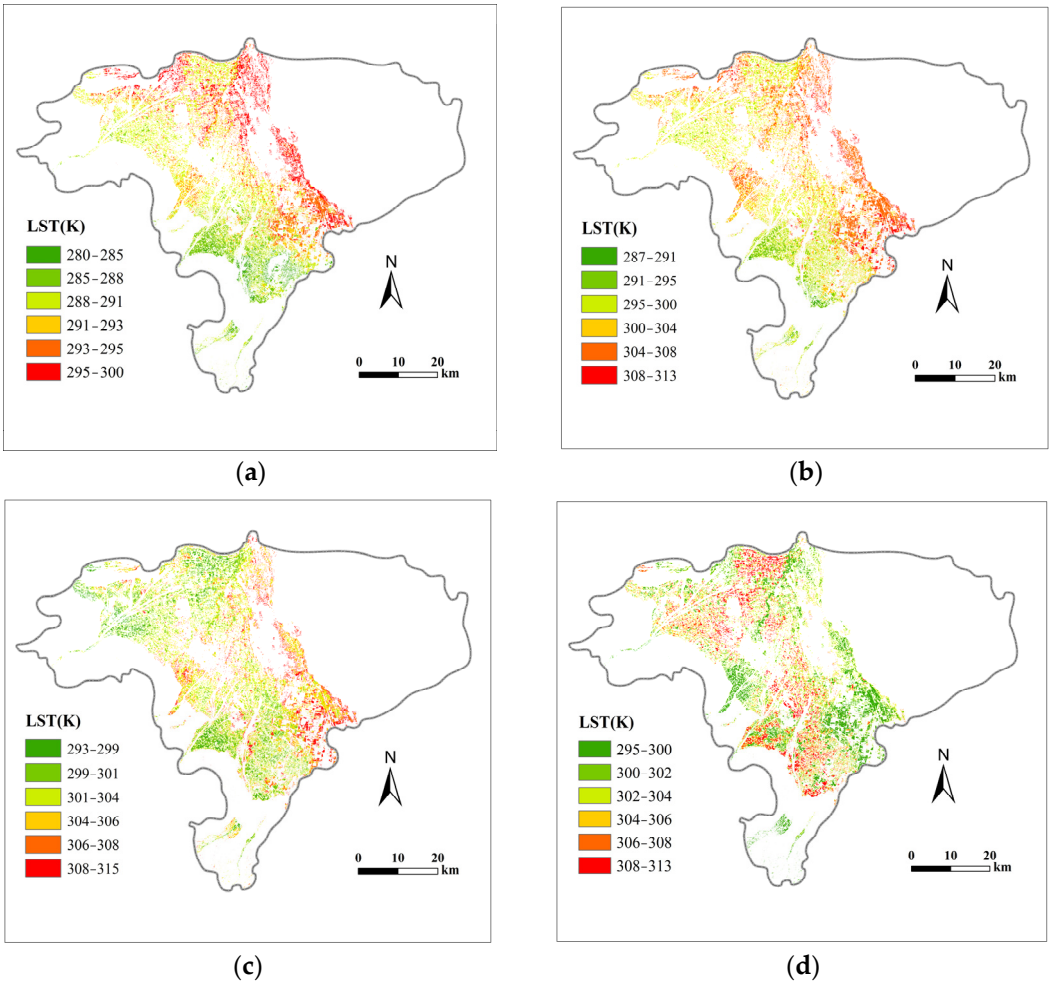
(**a**) (**b**)

Figure 7. *Cont.*



(**c**) (**d**)

Figure 7. Estimation results for the normalized difference vegetation index (NDVI): (**a**) the result from 12 May 2019; (**b**) the result from 28 May 2019; (**c**) the result from 13 June 2019; and (**d**) the result from 1 September 2019.



(**a**) (**b**)

(**c**) (**d**)

Figure 8. Estimation results for the land surface temperature (LST): (**a**) the result from 12 May 2019; (**b**) the result from 28 May 2019; (**c**) the result from 13 June 2019; and (**d**) the result from 1 September 2019.

3.2.2. Variation of Evapotranspiration

Significant spatial and temporal heterogeneity exists in the ET values across the region. The ET frequencies (Figures 9 and 10) reveal that the peak of the ET curve shifted backward with crop growth and approached a bimodal shape in each period, with the two peaks representing the wheat and corn zones, respectively. During May and June, ET was higher in the wheat distribution area, with the phenomenon being most pronounced in June. The daily ET peaks on 28 May and 13 June were 2.4 mm/d and 4.0 mm/d, and 2.0 mm/d and 5.2 mm/d, respectively. The left peak represents ET in the corn zone, while the right peak represents ET for wheat.

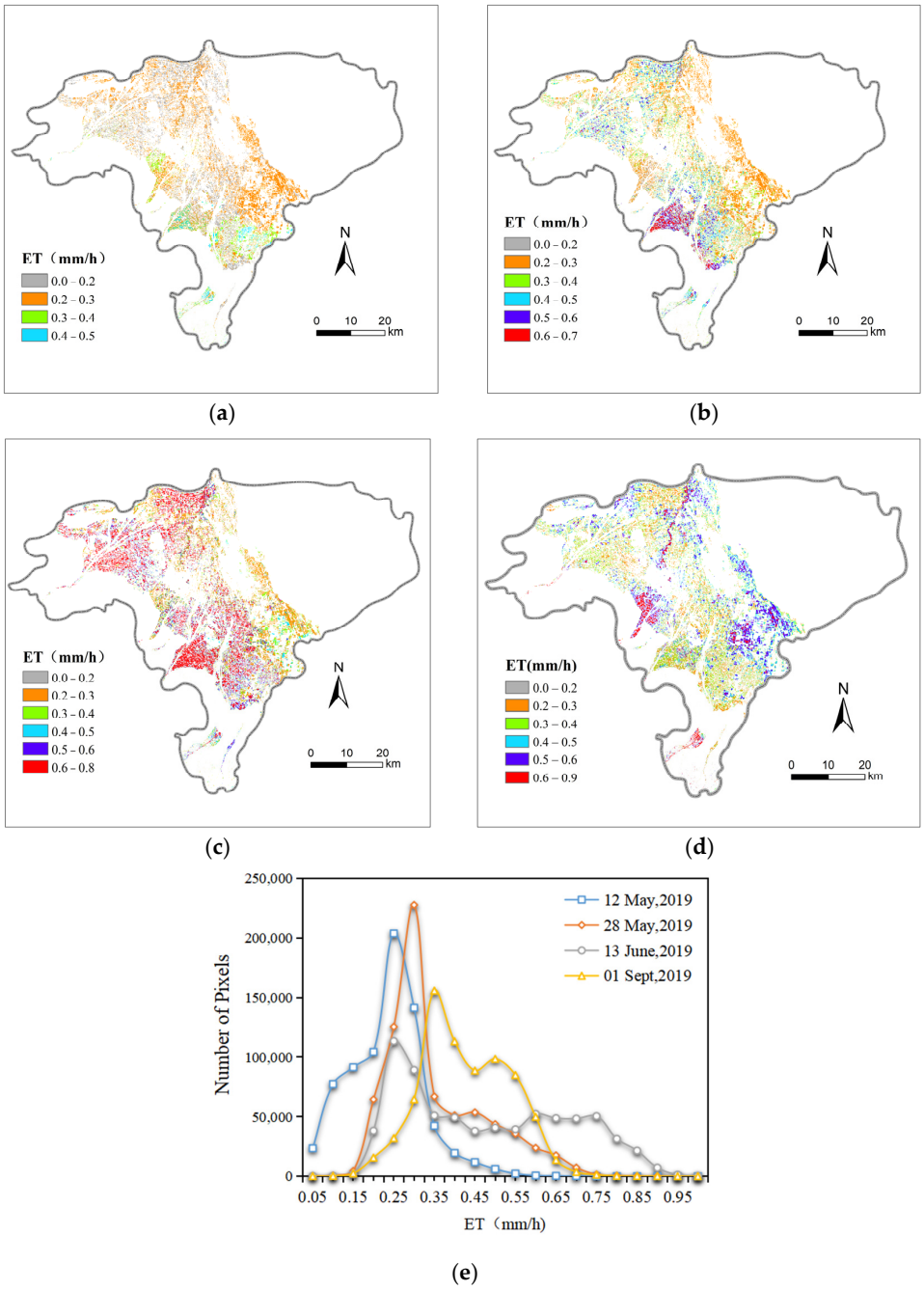


Figure 9. Estimation results for evapotranspiration (ET, mm/h): (**a**) the result from 12 May 2019; (**b**) the result from 28 May 2019; (**c**) the result from 13 June 2019; (**d**) the result from 1 September 2019; and (**e**) represents the instantaneous ET frequency map in each period.

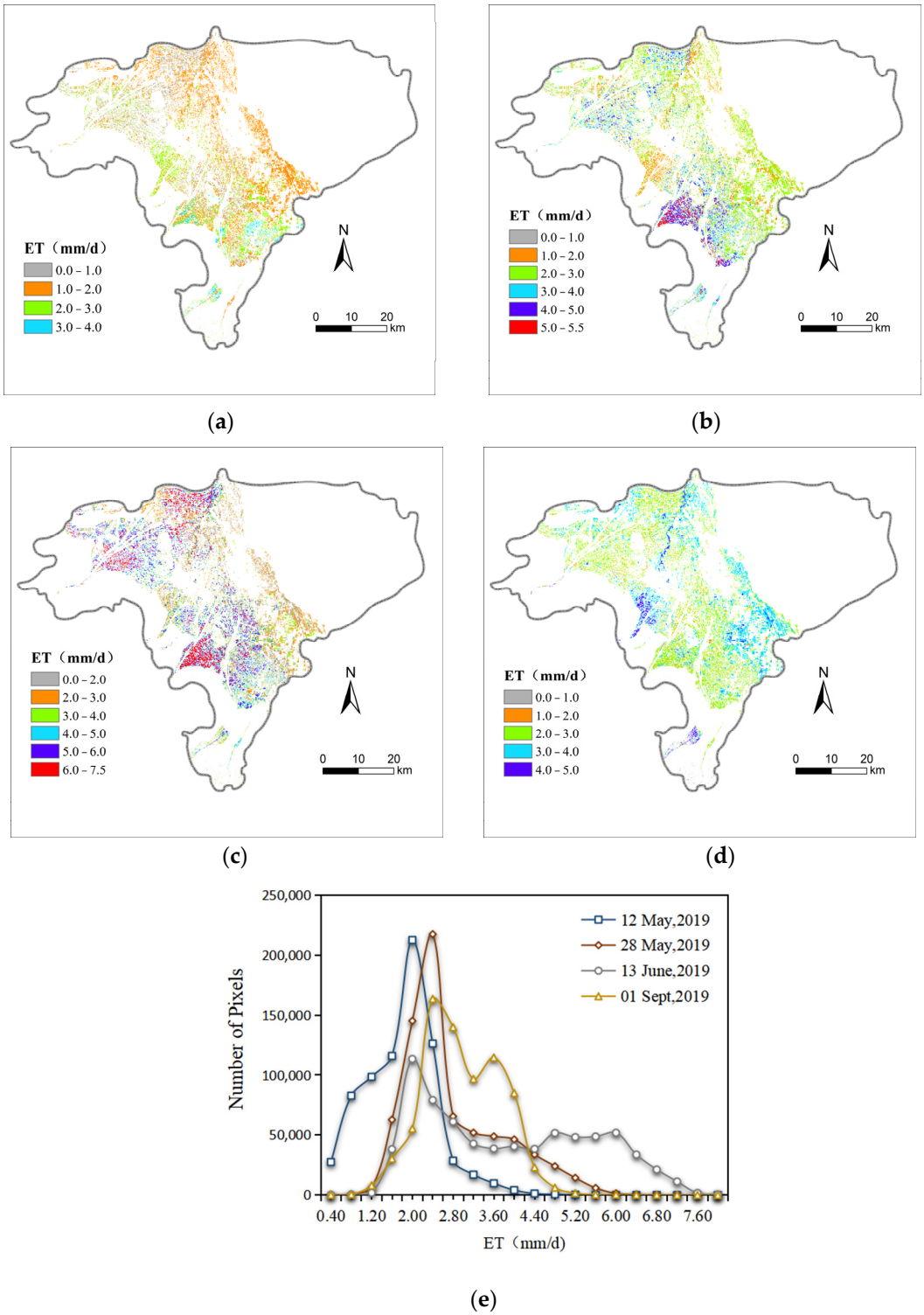


Figure 10. Estimation results for evapotranspiration (ET, mm/d): (**a**) the result from 12 May 2019; (**b**) the result from 28 May 2019; (**c**) the result from 13 June 2019; (**d**) the result from 1 September 2019; and (**e**) represents the frequency of daily ET in each period.

Figure 11 presents images from the same period in 2020, selected to illustrate the interannual variation of ET. The model parameters were obtained in the same manner and substituted into the 3T model to derive the daily ET values on 24 June 2020. This reveals an overall decrease in daily crop ET, with a maximum value of 4.0 mm/d compared to 13 June 2019. This decrease is significantly correlated with the later fertility of wheat and

corn in 2020 as opposed to 2019. However, ET levels increased in the corn range compared to 2019, and the effects of changes in climatic factors such as temperature must be taken into account. Consequently, the following analysis examines the primary factors affecting ET in terms of both climate and crop planting structures.

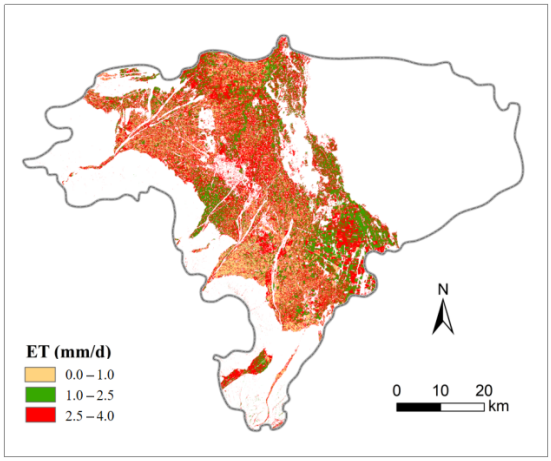


Figure 11. Daily evapotranspiration (ET) results for 24 June 2020.

3.3. The Response of Evapotranspiration to Planting Structure Factors

In order to better understand the difference in emission caused by different crop types in each period, the study extracted wheat and corn areas for mask analysis. Significant spatial heterogeneity is observed in the ET of both wheat and corn, which correlates with the NDVI and LST. Figures 12 and 13 depict the instantaneous ET obtained by substituting each parameter from the estimation into the 3T model, as well as the daily values of ET, acquired through the daily scale expansion of ET as proposed by Jackson et al. [50].

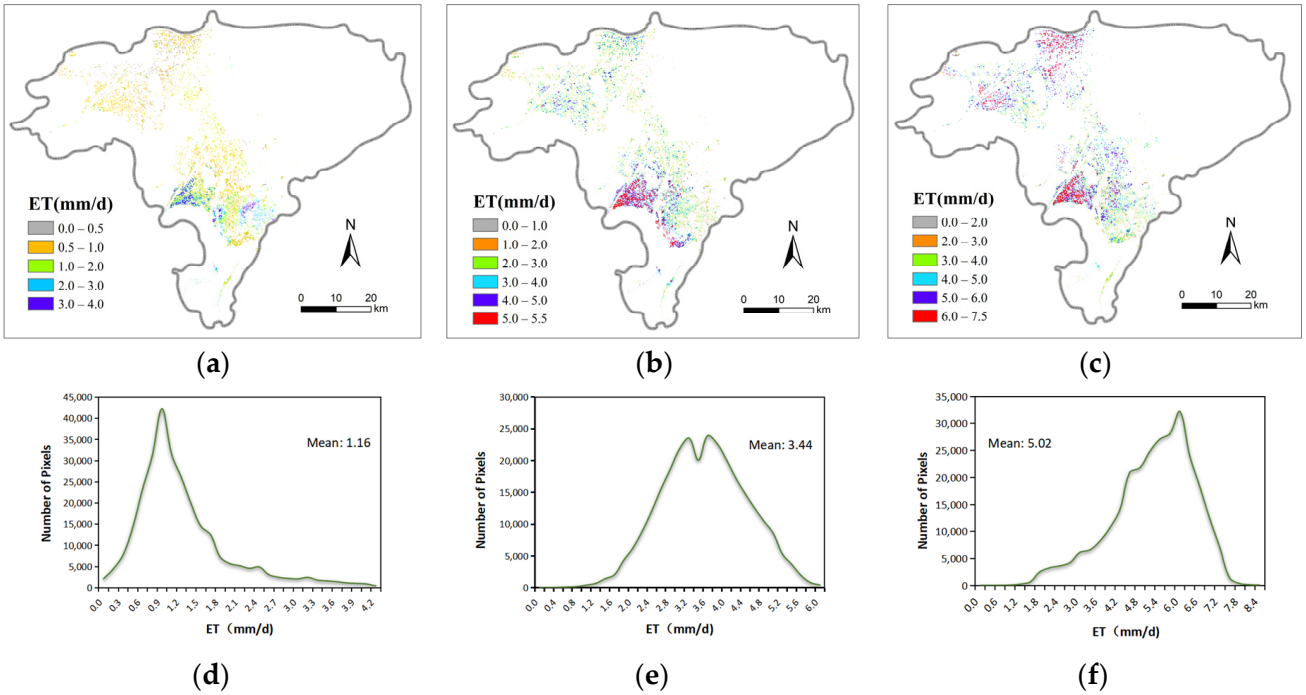


Figure 12. Daily evapotranspiration (ET) extracted by mask in the wheat area (mm/d): (**a**) the result from 12 May 2019; (**b**) the result from 28 May 2019; and (**c**) the result from 13 June 2019. Since the wheat was harvested in September, no date from the month is analyzed here. Finally, (**d**–**f**) represent the frequency of daily ET on the corresponding dates.

The spatial distribution in May is significantly different. The daily ET value of the wheat area was 0.40–2.00 mm/d on 12 May and 2.00–5.50 mm/d on 28 May. The difference in spatial distribution decreased in June, and the ET of the whole area was relatively concentrated. The daily ET on 13 June was 4.20–7.20 mm/d. According to the time distribution characteristics, the wheat ET increased from May to June and showed a gradual deepening of color from the spatial distribution map. On 12 May, 28 May, and 13 June, the average daily ET in the study area was 1.16 mm/d, 3.44 mm/d, and 5.02 mm/d, respectively.

In May, the spatial difference in ET distribution in the corn area is slight compared with the wheat area. On 12 May, the daily ET value of the corn area was 1.50~2.50 mm/d, and the value was 1.50~2.60 mm/d on 28 May. In June and September, the spatial difference increased. The daily ET in the corn area was 1.50~4.00 mm/d on 13 June and 2.00~4.40 mm/d on 1 September. On 12 May, 28 May, 13 June, and 1 September, the average daily ET of corn in the study area was 1.87 mm/d, 2.03 mm/d, 2.80 mm/d, and 3.20 mm/d, respectively. From the frequency distribution plots, it can be observed that both wheat and corn exhibit a rightward shift in their peak values over time. Additionally, there are notable differences in ET among different crops during the same period, which can effectively distinguish them. The findings considering the crop structure provide a scientific basis for precise irrigation.

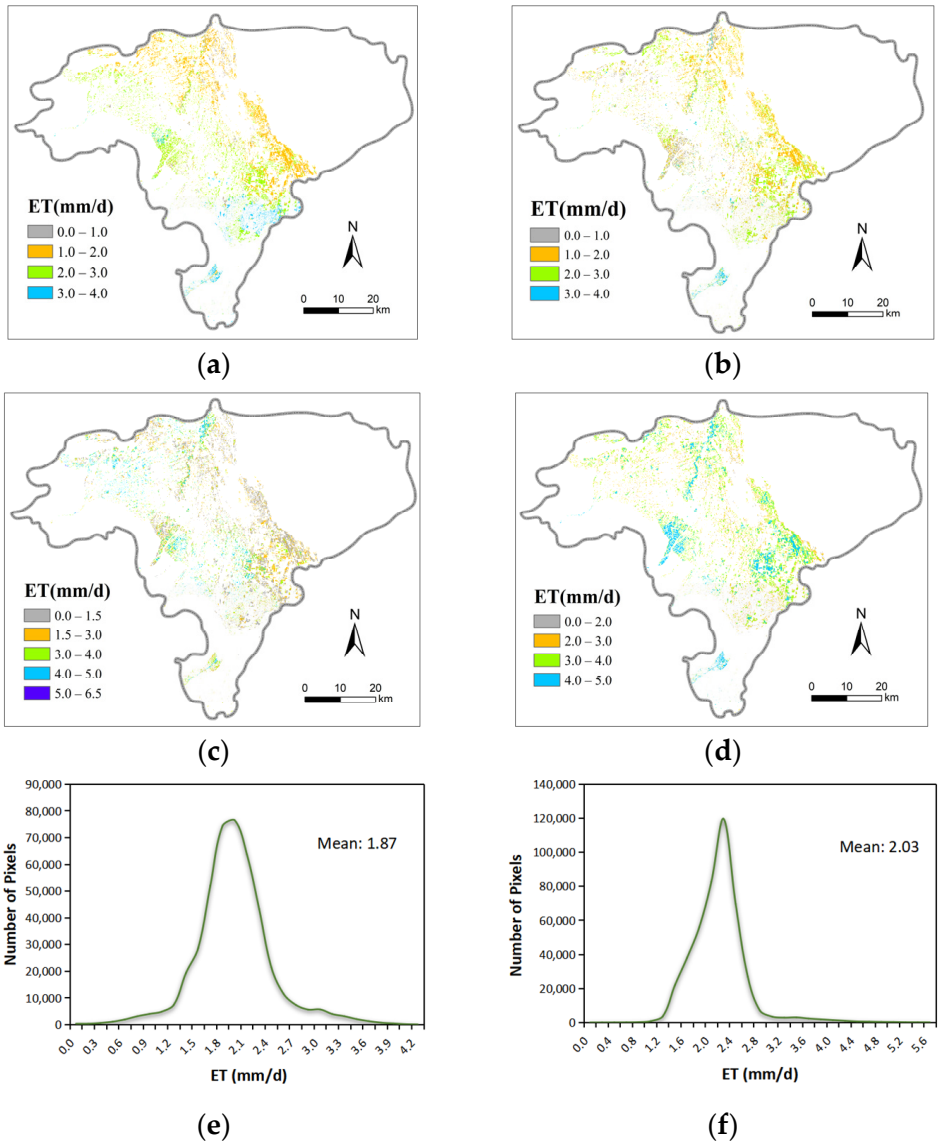
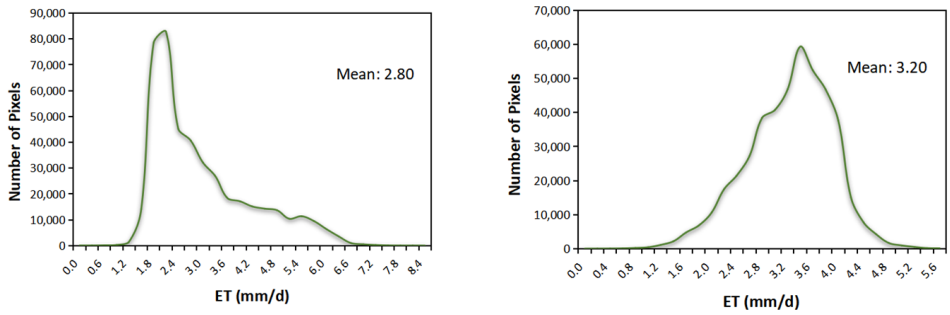


Figure 13. *Cont.*



(**g**) (**h**)

Figure 13. Daily evapotranspiration (ET) extracted by mask in the corn area (mm/d): (**a**) the result from 12 May 2019; (**b**) the result from 28 May 2019; (**c**) the result from 13 June 2019; (**d**) the result from 1 September 2019; and (**e**–**h**) represent the frequency of daily ET on the corresponding dates.

3.4. The Response of Evapotranspiration to Climatic Factors

The Pearson correlation analysis was conducted using the remotely sensed ET obtained during the typical days of the crop-growing seasons in 2019 and 2020 and the corresponding climatic factors of the respective years (Figure 14). From the results of the color-coded correlation matrices for interannual variation, it can be seen that Ta is the main factor affecting the change in ET and the correlation reaches 0.80 ($R = 0.80$, $p < 0.05$). Moreover, P also has a certain impact on ET, but the correlation is only 0.57 ($R = 0.57$, $p < 0.05$). This is because the agricultural fields in the study area are irrigated croplands, where crop growth relies entirely on artificial irrigation. Additionally, the study area is located in the Shiyang River Basin, which is characterized by limited and highly localized precipitation. Meanwhile, the correlation between the VPD and ET was only 0.21 ($R = 0.21$), which is consistent with the findings of Jin et al. [25]. They observed that VPD has only a slight influence on transpiration, while solar radiation plays a dominant role in atmospheric exchanges and serves as the primary driving force behind the spatial distribution of ET.



Figure 14. The color-coded correlation matrices for ET interannual variation.

4. Discussion

4.1. The Influence of Input Spectral Bands on the Identification of Crop Planting Structures

The choice of spectral bands for the satellite identification of planting structures should depend on several factors, including the resolution and availability of data, and the types

of crops being analyzed. Our results suggest that a more efficient band combination can improve the accuracy of crop classification. Combining the green and SWIR-1 bands is often a practical choice for the identification of planting structures in a watershed [52].

The green band is sensitive to chlorophyll and leaf area, providing information on the vegetation cover and its structure. The SWIR-1 band is sensitive to the water and structural properties of vegetation, providing information on the water content and structure of the canopy [53–55]. Meanwhile, increasing the number of bands or features in the classification does not necessarily improve the classification accuracy. Prior researchers have found that the information redundancy between variables increases the computational complexity and limits any improvement in accuracy, which is consistent with our findings [56].

4.2. The Influence of the Spatial Heterogeneity of Planting Structures on Evapotranspiration

In many irrigated agricultural areas, different crops are staggered and the fields are irregular and fragmented, resulting in sharp spatial fluctuations in parameters such as ET, soil moisture, and LST [28]. Most existing estimation models neglect the physiological characteristics arising from significant differences in water conditions among different crops [57,58]. According to the results of the planting structure analysis, the planted area of major cash crops decreased by 4.536 kha in 2020 compared to 2019, which contributed to the reduction in ET in 2020. From the input parameters of the 3T model, notable differences in key ET estimation features were observed between wheat and corn. In June, wheat exhibited higher ET levels in its distribution area due to being in the middle to late stages of the growth period, with maximum vegetation coverage of 1.0. Meanwhile, corn was still in the early stage of the elongation period in mid-June. Wheat in the LD is harvested around 20 July, after which the wheat area is fallowed or rotated with crops such as baby bok choy by 1 September while corn reaches its maturity stage. At this time, corn exhibits the highest levels of ET throughout its growth period, with a daily value of 3.20 mm/d. The findings demonstrate the significance of conducting crop classification with remote sensing estimation for crop moisture status monitoring.

In Section 3, as a representative crop of typical crops with significant differences in water consumption, we created the mask from the results of crop planting structure classification for the wheat and corn, respectively, and found that the ET estimation results were most influenced by the crop type based on the image element properties. However, from the frequency distribution chart of ET (Figures 12 and 13), it can be observed that the value of ET of the two crops is not sufficiently concentrated, with distribution in various ranges (number of pixels > 5000), indicating the presence of some errors in the estimation of ET results. Two main factors are causing the errors: first, there are some discrepancies between the wheat and corn planting structures extracted from the remote sensing images and the field planting situation, and the fragmented plots that do not belong to both have been mistakenly identified as well. Second, due to the limitation of the resolution of Landsat-8 data, there is a phenomenon of mixed pixels. Therefore, the values with a more concentrated frequency were selected when analyzing the estimation results for practical application. The anomalous marginal values were discarded to reduce the interference of the anomalous values.

4.3. The Influence of Meteorological Factors on the Estimation of Evapotranspiration

Ta is a relatively stable environmental factor, and this study considers it the main meteorological factor influencing the spatiotemporal variation of ET. The increase in temperature promotes the evaporation rate of soil moisture from the crop surface and the topsoil, resulting in more water entering the atmosphere through faster evaporation. In the study conducted by Jun et al. [59] in Lanzhou, the meteorological factors considered were net radiation, air temperature, and relative humidity. Their results reveal a significant relationship between air temperature and crop evapotranspiration, with an R^2 of 0.789. Meanwhile, Gao's study indicates a strong correlation between temperature variations and field ET during the crop growth period, with a coefficient of determination exceeding 0.9 [60]. In addition, Rigden et al. [61] demonstrated that on longer time scales, variations

in precipitation among meteorological factors had the most prominent impact on the partitioning of ET. The changes in soil moisture resulting from precipitation also exerted a significant influence on ET, but the correlation was lower (R = 0.57). A typical feature of the Shiyang River Basin is low precipitation, and the precipitation events are highly localized, especially in the crop-growing season. However, for the irrigated farmland in the LD, the supply of precipitation is far from sufficient to support crop growth.

5. Conclusions

Planting structure identification in the LD was investigated in this study using multispectral and multi-temporal Landsat-8 images. A novel quantitative characterization of the response of ET to climate and planting structures was achieved, and the detailed conclusions indicate the following:

(1) Using a random forest classifier, a combination of the green and SWIR-1 bands from multi-temporal Landsat-8 images was found to be the optimal feature set to extract the crop planting structures in the LD. The wheat planting areas were 31.594 kha and 24.241 kha in 2019 and 2020, respectively, while the corn areas were 44.505 kha and 47.322 kha for those same years. The accuracy of the planting structure classification results ranged from 85.82% to 98.25%.

(2) The integration of crop planting structures with the 3T model enhanced the realism and reliability of ET estimation. The spatial differences between the two crops were more pronounced from June to September. Among the four selected dates, the average daily ET in the wheat area was 1.16 mm/d, 3.44 mm/d, and 5.02 mm/d, respectively (wheat was harvested around 20 July). While in the corn area, it was 1.87 mm/d, 2.03 mm/d, 2.80 mm/d, and 3.20 mm/d, respectively.

(3) Concerning the climatic factors considered in this study, ET's spatiotemporal variations were primarily driven by Ta (R = 0.80, $p \leq 0.05$). The research quantified the contributions of crop planting structures and climate factors to variations in ET, providing a basis for better understanding the impact of crop planting structure on remote sensing-based ET estimation. However, this study focused on major cash crops, and further exploration is needed to investigate the effects of more refined and diverse crop planting structures on ET using remote sensing techniques.

Author Contributions: Conceptualization, X.Y., X.S., Y.Z. and F.T.; data curation, X.S. and F.T.; formal analysis, X.Y. and X.S.; funding acquisition, F.T.; investigation, X.Y., X.S. and Y.Z.; methodology, X.Y., X.S., Y.Z. and F.T.; project administration, F.T.; software, X.Y.; supervision, F.T. and S.O.-F.; validation, X.Y., X.S., Y.Z. and F.T.; visualization, X.Y.; writing—original draft, X.Y.; writing—review and editing, F.T. All authors have read and agreed to the published version of the manuscript.

Funding: This work was supported by the international and regional cooperation and exchange projects of the National Natural Science Foundation of China (51961125205), the National Natural Science Foundation of China (52179049), the National Key R&D Program of China (2022YFD190050403), and the *Western Light*-Key Laboratory Cooperative Research Cross-Team Project of Chinese Academy of Sciences (xbzg-zdsys-202103).

Data Availability Statement: Not applicable.

Conflicts of Interest: All the authors declare no conflict of interest.

References

1. Liu, J.; You, Y.; Li, J.; Sitch, S.; Gu, X.; Nabel, J.E.M.S.; Lombardozzi, D.; Luo, M.; Feng, X.; Arneth, A.; et al. Response of global land evapotranspiration to climate change, elevated CO_2, and land use change. *Agric. For. Meteorol.* **2021**, *311*, 108663. [CrossRef]
2. Wei, Z.; Yoshimura, K.; Wang, L.; Miralles, D.G.; Jasechko, S.; Lee, X. Revisiting the contribution of transpiration to global terrestrial evapotranspiration. *Geophys. Res. Lett.* **2017**, *44*, 2792–2801. [CrossRef]
3. Kool, D.; Agam, N.; Lazarovitch, N.; Heitman, J.L.; Sauer, T.J.; Ben-Gal, A. A review of approaches for evapotranspiration partitioning. *Agric. For. Meteorol.* **2014**, *184*, 56–70. [CrossRef]
4. Soer, G.J.R. Estimation of Regional Evapotranspiration and Soft Moisture Conditions Using Remotely Sensed Crop Surface Temperatures. *Remote Sens. Environ.* **1980**, *9*, 27–45. [CrossRef]
5. Qiu, G.; Momii, K.; Yano, T. Estimation of Plant Transpiration by Imitation Leaf Temperature Theoretical consideration and filed verfication(I). *Trans. Jpn. Soc. Irrig. Drain. Reclam. Eng.* **1996**, *183*, 401–410.
6. Qiu, G.; Wang, S.; Wu, X. Three Temperature (3T) Model—A Method to Estimate Evapotranspiration and Evaluate Environmental Quality. *J. Plant Ecol.* **2006**, *30*, 231–238.
7. Tian, F.; Qiu, G.; Yang, Y.; Lü, Y.; Xiong, Y. Estimation of evapotranspiration and its partition based on an extended three-temperature model and MODIS products. *J. Hydrol.* **2013**, *498*, 210–220. [CrossRef]
8. Xiong, Y.; Zhao, S.; Tian, F.; Qiu, G. An evapotranspiration product for arid regions based on the three-temperature model and thermal remote sensing. *J. Hydrol.* **2015**, *530*, 392–404. [CrossRef]
9. Hou, M.; Tian, F.; Zhang, L.; Li, S.; Du, T.; Huang, M.; Yuan, Y. Estimating Crop Transpiration of Soybean under Different Irrigation Treatments Using Thermal Infrared Remote Sensing Imagery. *Agronomy* **2019**, *9*, 8. [CrossRef]
10. Piao, S.; Friedlingstein, P.; Ciais, P.; de Noblet-Ducoudré, N.; Labat, D.; Zaehle, S. Changes in climate and land use have a larger direct impact than rising CO_2 on global river runoff trends. *Proc. Natl. Acad. Sci. USA* **2007**, *104*, 15242–15247. [CrossRef]
11. Zhang, Y.; Qiu, G.; Yan, C.; Wen, H. Studies on the influence of altitudes on the trend of reference evapotranspiration in recent 50 years: A case study of Sichuan province. *Ecol. Environ. Sci.* **2018**, *27*, 2208–2216.
12. Qiu, M.; Liu, B.; Liu, Y.; Zhang, Y.; Wu, X.; Yuan, F.; Wang, D.; Mu, C. Temporal -Spatial Variation Characteristics of Reference Crop Evapotranspiration and Its Influence Factors in Jilin Province. *J. Arid Environ.* **2019**, *37*, 119–126.
13. Li, Y.; Zhang, L.; Cao, Y. Spatiotemporal variation characteristics of potential evapotranspiration and climate influencing factors in Hebei province. *South-North Water Transf. Water Sci. Technol.* **2019**, *17*, 67–78.
14. Liu, X.; Zheng, H.; Zhang, M.; Liu, C. Identification of dominant climate factor for pan evaporation trend in the Tibetan Plateau. *J. Geogr. Sci.* **2011**, *21*, 594–608. [CrossRef]
15. Jin, Z.; Liang, W.; Yang, Y.; Zhang, W.; Yan, J.; Chen, X.; Li, S.; Mo, X. Separating Vegetation Greening and Climate Change Controls on Evapotranspiration trend over the Loess Plateau. *Sci. Rep.* **2017**, *7*, 1–15. [CrossRef]
16. He, G.; Zhao, Y.; Wang, J.; Gao, X.; He, F.; Li, H.; Zhai, J.; Wang, Q.; Zhu, Y. Attribution analysis based on Budyko hypothesis for land evapotranspiration change in the Loess Plateau, China. *J. Arid Land* **2019**, *11*, 939–953. [CrossRef]
17. Bolton, D.K.; Friedl, M.A. Forecasting crop yield using remotely sensed vegetation indices and crop phenology metrics. *Agric. For. Meteorol.* **2013**, *173*, 74–84. [CrossRef]
18. Kang, S. Towards water and food security in China. *Chin. J. Eco-Agric.* **2014**, *22*, 880–885.
19. Yang, F.; Matsushita, B.; Yang, W.; Fukushima, T. Mapping the human footprint from satellite measurements in Japan. *Isprs-J. Photogramm. Remote Sens.* **2014**, *88*, 80–90. [CrossRef]
20. Chen, H.; Qiu, Y.; Yin, D.; Chen, J.; Chen, X.; Liu, S.; Liu, L. Stacked spectral feature space patch: An advanced spectral representation for precise crop classification based on convolutional neural network. *Crop J.* **2022**, *10*, 1460–1469. [CrossRef]
21. Biradar, C.M.; Xiao, X. Quantifying the area and spatial distribution of double- and triple-cropping croplands in India with multi-temporal MODIS imagery in 2005. *Int. J. Remote Sens.* **2011**, *32*, 367–386. [CrossRef]
22. Dong, J.; Xiao, X.; Menarguez, M.A.; Zhang, G.; Qin, Y.; Thau, D.; Biradar, C.; Moore, B. Mapping paddy rice planting area in northeastern Asia with Landsat 8 images, phenology-based algorithm and Google Earth Engine. *Remote Sens. Environ.* **2016**, *185*, 142–154. [CrossRef] [PubMed]
23. Gao, F.; Anderson, M.C.; Zhang, X.; Yang, Z.; Alfieri, J.G.; Kustas, W.P.; Mueller, R.; Johnson, D.M.; Prueger, J.H. Toward mapping crop progress at field scales through fusion of Landsat and MODIS imagery. *Remote Sens. Environ.* **2017**, *188*, 9–25. [CrossRef]
24. Wardlow, B.D.; Egbert, S.L. Large-area crop mapping using time-series MODIS 250 m NDVI data: An assessment for the U.S. Central Great Plains. *Remote Sens. Environ.* **2008**, *112*, 1096–1116. [CrossRef]
25. Xiao, X.; Boles, S.; Liu, J.; Zhuang, D.; Frolking, S.; Li, C.; Salas, W.; Moore, B. Mapping paddy rice agriculture in southern China using multi-temporal MODIS images. *Remote Sens. Environ.* **2005**, *95*, 480–492. [CrossRef]
26. Konduri, V.S.; Kumar, J.; Hargrove, W.W.; Hoffman, F.M.; Ganguly, A.R. Mapping crops within the growing season across the United States. *Remote Sens. Environ.* **2020**, *251*, 112048. [CrossRef]
27. You, N.; Dong, J. Examining earliest identifiable timing of crops using all available Sentinel 1/2 imagery and Google Earth Engine. *Isprs-J. Photogramm. Remote Sens.* **2020**, *161*, 109–123. [CrossRef]
28. Wang, S.; Wang, C.; Zhang, C.; Xue, J.; Wang, P.; Wang, X.; Wang, W.; Zhang, X.; Li, W.; Huang, G.; et al. A classification-based spatiotemporal adaptive fusion model for the evaluation of remotely sensed evapotranspiration in heterogeneous irrigated agricultural area. *Remote Sens. Environ.* **2022**, *273*, 112962. [CrossRef]

29. Mankin, J.S.; Seager, R.; Smerdon, J.E.; Cook, B.I.; Williams, A.P. Mid-latitude freshwater availability reduced by projected vegetation responses to climate change. *Nat. Geosci.* **2019**, *12*, 983–988. [CrossRef]
30. Chintala, S.; Harmya, T.S.; Kambhammettu, B.V.N.P.; Moharana, S.; Duvvuri, S. Modelling high-resolution Evapotranspiration in fragmented croplands from the constellation of Sentinels. *Remote Sens. Appl. Soc. Environ.* **2022**, *26*, 100704. [CrossRef]
31. Tran, K.H.; Zhang, H.K.; McMaine, J.T.; Zhang, X.; Luo, D. 10 m crop type mapping using Sentinel-2 reflectance and 30 m cropland data layer product. *Int. J. Appl. Earth Obs. Geoinf.* **2022**, *107*, 102692. [CrossRef]
32. Wardlow, B.D.; Egbert, S.L.; Kastens, J.H. Analysis of time-series MODIS 250 m vegetation index data for crop classification in the U.S. Central Great Plains. *Remote Sens. Environ.* **2007**, *108*, 290–310. [CrossRef]
33. Duro, D.C.; Franklin, S.E.; Dubé, M.G. A comparison of pixel-based and object-based image analysis with selected machine learning algorithms for the classification of agricultural landscapes using SPOT-5 HRG imagery. *Remote Sens. Environ.* **2012**, *118*, 259–272. [CrossRef]
34. Cai, Y.; Guan, K.; Peng, J.; Wang, S.; Seifert, C.; Wardlow, B.; Li, Z. A high-performance and in-season classification system of field-level crop types using time-series Landsat data and a machine learning approach. *Remote Sens. Environ.* **2018**, *210*, 35–47. [CrossRef]
35. Zhong, L.; Gong, P.; Biging, G.S. Efficient corn and soybean mapping with temporal extendability: A multi-year experiment using Landsat imagery. *Remote Sens. Environ.* **2014**, *140*, 1–13. [CrossRef]
36. Zhong, L.; Hu, L.; Zhou, H. Deep learning based multi-temporal crop classification. *Remote Sens. Environ.* **2019**, *221*, 430–443. [CrossRef]
37. Xiong, J.; Thenkabail, P.S.; Gumma, M.K.; Teluguntla, P.; Poehnelt, J.; Congalton, R.G.; Yadav, K.; Thau, D. Automated cropland mapping of continental Africa using Google Earth Engine cloud computing. *Isprs-J. Photogramm. Remote Sens.* **2017**, *126*, 225–244. [CrossRef]
38. Chen, M.; Li, C.; Guan, Y.; Zhou, J.; Wang, D.; Luo, Z. Generation and application of high temporal and spatial resolution images of regional farmland based on ESTARFM model. *Acta Agron. Sin.* **2019**, *45*, 1099–1110.
39. Qiu, G.; Yano, T.; Momii, K. An improved methodology to measure evaporation from bare soil based on comparison of surface temperature with a dry soil surface. *J. Hydrol.* **1998**, *210*, 93–105. [CrossRef]
40. Lu, S.; Xuan, J.; Zhang, T.; Bai, X.; Tian, F.; Ortega-Farias, S. Effect of the Shadow Pixels on Evapotranspiration Inversion of Vineyard: A High-Resolution UAV-Based and Ground-Based Remote Sensing Measurements. *Remote Sens.* **2022**, *14*, 2259. [CrossRef]
41. Tian, F.; Qiu, G.; Lü, Y.; Yang, Y.; Xiong, Y. Use of high-resolution thermal infrared remote sensing and "three-temperature model" for transpiration monitoring in arid inland river catchment. *J. Hydrol.* **2014**, *515*, 307–315. [CrossRef]
42. Qiu, G.; Momii, K.; Yano, T. Estimation of plant transpiration by imitation leaf temperature. II. Application of imitation leaf temperature for detection of crop water stress. *Trans. Jpn. Soc. Irrig. Drain. Reclam. Eng.* **1996**, *185*, 767–773.
43. Qiu, G.; Shi, P.; Wang, L. Theoretical analysis of a remotely measurable soil evaporation transfer coefficient. *Remote Sens. Environ.* **2006**, *101*, 390–398. [CrossRef]
44. Walthall, C. A comparison of empirical and neural network approaches for estimating corn and soybean leaf area index from Landsat ETM+ imagery*1. *Remote Sens. Environ.* **2004**, *92*, 465–474. [CrossRef]
45. Artis, D.A.; Carnahan, W.H. Survey of Emissivity Variability in Thennography of Urban Areas. *Remote Sens. Environ.* **1982**, *12*, 313–329. [CrossRef]
46. Monteith, J.L. Solar Radiation and Productivity in Tropical Ecosystems. *J. Appl. Ecol.* **1972**, *9*, 747–766. [CrossRef]
47. Kustas, W.P.; Daughtry, C.S.T. Estimation of the soil heat flux/net radiation ratio from spectral data. *Agric. For. Meteorol.* **1990**, *49*, 205–223. [CrossRef]
48. Sobrino, J.A.; Jiménez-Muñoz, J.C.; Paolini, L. Land surface temperature retrieval from LANDSAT TM 5. *Remote Sens. Environ.* **2004**, *90*, 434–440. [CrossRef]
49. Xiong, Y.; Qiu, G.Y. Estimation of evapotranspiration using remotely sensed land surface temperature and the revised three-temperature model. *Int. J. Remote Sens.* **2011**, *20*, 5853–5874. [CrossRef]
50. Jackson, R.D.; Hatfield, J.L.; Reginato, R.J.; Idso, S.B.; Pinter, P.J., Jr. Estimation of daily evapotranspiration from one time-of-day measurements. *Agric. Water Manag.* **1983**, *7*, 351–362. [CrossRef]
51. Benesty, J.; Chen, J.; Huang, Y.; Cohen, I. *Pearson Correlation Coefficient. Noise Reduction in Speech Processing. Springer Topics in Signal Processing*, 2nd ed.; Springer: Berlin/Heidelberg, Germany, 2009; pp. 1–4.
52. Hively, W.D.; Lamb, B.T.; Daughtry, C.S.T.; Serbin, G.; Dennison, P.; Kokaly, R.F.; Wu, Z.; Masek, J.G. Evaluation of SWIR Crop Residue Bands for the Landsat Next Mission. *Remote Sens.* **2021**, *13*, 3718. [CrossRef]
53. Yilmaz, M.T.; Hunt, E.R.; Jackson, T.J. Remote sensing of vegetation water content from equivalent water thickness using satellite imagery. *Remote Sens. Environ.* **2008**, *112*, 2514–2522. [CrossRef]
54. Feng, S.; Zhao, J.; Liu, T.; Zhang, H.; Zhang, Z.; Guo, X. Crop Type Identification and Mapping Using Machine Learning Algorithms and Sentinel-2 Time Series Data. *Ieee J. Sel. Top. Appl. Earth Observ. Remote Sens.* **2019**, *12*, 3295–3306. [CrossRef]
55. Ghulam, A.; Li, Z.; Qin, Q.; Yimit, H.; Wang, J. Estimating crop water stress with ETM+ NIR and SWIR data. *Agric. For. Meteorol.* **2008**, *148*, 1679–1695. [CrossRef]
56. Camps-Va, G.; Mooij, J.; Scholkopf, B. Remote Sensing Feature Selection by Kernel Dependence Measures. *IEEE Geosci. Remote Sens. Lett.* **2010**, *7*, 587–591. [CrossRef]
57. Norman, J.M.; Kustas, W.P.; Humes, K.S. Source approach for estimating soil and vegetation energy fluxes in observations of directional radiometric surface temperature. *Agric. For. Meteorol.* **1995**, *77*, 263–293. [CrossRef]

58. Long, D.; Singh, V.P. A modified surface energy balance algorithm for land (M-SEBAL) based on a trapezoidal framework. *Water Resour. Res.* **2012**, *48*. [CrossRef]
59. Jun, D. Studies on Stomatal Conductance and Evapotranspiration of Maize Field in Semi-Arid Area. Master's Thesis, Lanzhou University, Lanzhou, China, 2017.
60. Gao, H. Water and Energy Balance of Irrigated Field in the Middle Basis Oasis of Heihe River. Ph.D. Thesis, The University of Chinese Academy of Sciences, Beijing, China, 2015.
61. Rigden, A.J.; Salvucci, G.D.; Entekhabi, D.; Short Gianotti, D.J. Partitioning Evapotranspiration Over the Continental United States Using Weather Station Data. *Geophys. Res. Lett.* **2018**, *45*, 9605–9613. [CrossRef]

Disclaimer/Publisher's Note: The statements, opinions and data contained in all publications are solely those of the individual author(s) and contributor(s) and not of MDPI and/or the editor(s). MDPI and/or the editor(s) disclaim responsibility for any injury to people or property resulting from any ideas, methods, instructions or products referred to in the content.